Regular Article

Competing twinning mechanisms in body-centered cubic metallic nanowires

Zhe Shi, Chandra Veer Singh *

Department of Materials Science and Engineering, University of Toronto, 184 College St., Toronto, Ontario M5S 3E4, Canada

ARTICLE INFO

ABSTRACT

Twinning in body-centered cubic metals is typically attributed to glide of 1/6<111> dislocations originated from material defects. Here we report an alternative mechanism for twin formation in body-centered cubic nanowires using molecular dynamics simulations. In this mechanism, twinning is triggered by dissociation of the 1/6<111> dislocation into two 1/12<111> partials gliding on adjacent {211} planes. By comparing the generalized stacking fault energies of the two competing twin boundary configurations in five different BCC crystals, the propensity of a particular mechanism to occur is evaluated. The fundamental insight gained from this study will help engineer nanoscale materials with novel mechanical properties.

© 2015 Elsevier B.V. All rights reserved.

The mechanical response of metallic nanostructures has been the focus of intense research in recent years due to their superior strengths and unique deformation behaviors. With no preexisting dislocations, a nanowire (NW) or nanowhisker is able to possess near-ideal strength and deforms by nucleating dislocations from its free surfaces [1–7], leading to what is known as the "smaller is stronger" phenomenon [8–10]. During the deformation, twinning is commonly observed to occur due to readily achieved high stresses resulted from the exhaustion of dislocation sources [2,5,6]. In particular for the body-centered cubic (BCC) NWs, the twinning is also known to be responsible for the pseudoplasticity and shape memory effect [11–13]. A fundamental understanding of twinning is thus essential to enable nanostructured designs that fully manifest latent strength of BCC metals, with promising applications in areas such as energy storage [14].

Recently, in situ observation of deformation twins in BCC tungsten nanowires was reported [10], wherein twinning was suggested to occur by the nucleation of 1/6<111> partial dislocations and their subsequent glide on {211} atomic planes. Previous theoretical studies on BCC NWs have investigated this mechanism, whereby a conventional mirror symmetrical reflection twin boundary (TB) structure is formed [11,12]. However, from a conceptual perspective, an alternative "isosceles" TB structure that violates the mirror symmetry can also exist in BCC metals [15–17] (Fig. 1a). The formation of isosceles TB structure in BCC NWs and the energetics of the process have not been studied so far. Also, it is not clear which type of TB structure would prevail among different BCC systems. A TEM study of shock-induced phase transformation in tantalum suggested a 1/12<111> type of

displacement [18]. The similarity of high stress conditions in both shock impact and nanowire twinning inspires us to look into how dislocation glide would trigger the formation of the isosceles TB.

In this paper, we utilize molecular dynamics (MD) to report and investigate a unique twinning mechanism in BCC NWs occurring under uniaxial loading that drives the formation of the isosceles twin boundary, in contrast to the formation of the reflection TBs. By comparing twinning behavior and the associated generalized stacking fault energy curves for single crystal BCC niobium, iron, tantalum, molybdenum, and tungsten NWs, we also analyze the competition between these two twinning mechanisms, and predict the propensity of a particular mechanism over another in a given crystal.

The twinning deformation is conducted in each BCC NW by uniaxial loading along longitudinal direction at a constant strain rate of 10^8/s after relaxation at 0.1 K by using the Nosé–Hoover thermostat [19]. Three NW orientations were analyzed: <110>/{111}, <100>/{110}, and <100>/{100} (<loading direction>/{transverse surface}). All of the five types of BCC NWs have a dimension of $30a \times 30a \times 150a$, where a is the lattice constant, with free boundary conditions utilized to simulate NW transverse surfaces. The BCC metals were modeled by Finnis–Sinclair potential [20] or optimized EAM potentials [21–24] to agree well with DFT calculated or experimentally measured properties and energy values that are of our concern (see Supplementary Material, SM-II).

During deformation of the BCC NWs, two distinct twinning mechanisms were observed in all of the five NW systems studied here for all three NW orientations. In the first mechanism, known traditionally, 1/6<111> dislocations are nucleated from NW free surfaces and subsequently glide on {211} atomic planes to realize twinning deformation. In the second case, however, the 1/6<111> dislocation is observed to

* Corresponding author.
E-mail address: chandraveer.singh@utoronto.ca (C.V. Singh).
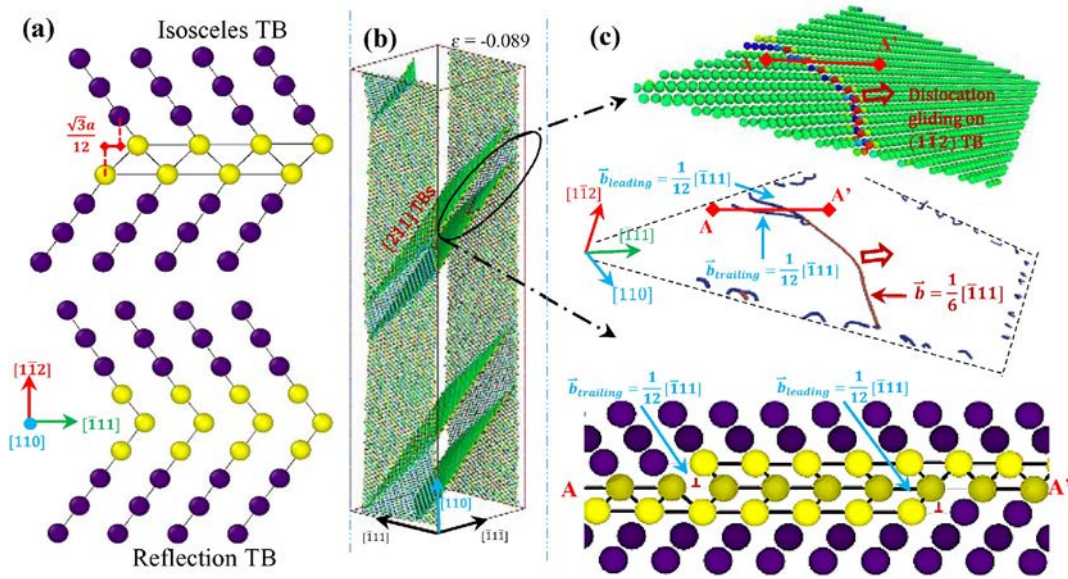
Fig. 1. Schematics for two TB structures in BCC crystals are shown in (a). During the twinning deformation of a <110>/{111} BCC Nb NW (b), a 1/6<111> dislocation on the $(1\bar{1}2)$ TB dissociates into two 1/12<111> partials, whose glide causes the formation of the asymmetrical isosceles TB structure (c). Snapshot of atomic configuration of Segment AA′ from the [110] direction is also presented in (c). All snapshots are from real MD simulations, processed using the OVITO [26] or ParaView [27] packages.

dissociate into two 1/12<111> partial dislocations which glide simultaneously on adjacent {211} planes in a subsequent manner to realize twinning. As shown in Fig. 1b & c, a section of a $\frac{1}{6}[\bar{1}11]$ dislocation in a <110>-oriented NW dissociates by: $\frac{1}{6}[\bar{1}11] = \frac{1}{12}[\bar{1}11] + \frac{1}{12}[\bar{1}11]$. Consequently, the conventional perfect mirror symmetrical (reflection) configuration is not maintained across the two sides of the TB. Instead, a unique TB consisting of the isosceles triangular configuration emerges. This is evident in Fig. 1c, where a TB having the isosceles structure at two sides and a reflection portion in the middle is formed during the glide of $1/12[\bar{1}11]$ dislocations. After these two dislocations completely pass through the NW, only the isosceles TB configuration is left. This mechanism was also found to hold at finite temperatures, lower strain

rate (10^7/s), larger NW sizes, and for circular cross-section, providing further support for its existence. A comprehensive rate dependence study as in Ref. [25] may be necessary to ascertain this mechanism at experimentally relevant rates. Moreover, this dissociation was preferred at the edges (Fig. 1c) for Nb NWs; this edge preference was not observed for W NWs (SM, Fig. S4), implying that this behavior is material dependent.

To understand the atomistic process causing formation of the isosceles TB structure, a step-by-step atomic motion is presented in Fig. 2. The simultaneous glide of the 1/12<111> dislocation pair can be thought equivalently to have two sub-steps, as depicted from Fig. 2a to b. The participating 1/12<111> dislocations are labeled as $\vec{b}_1$ and $\vec{b}_2$,
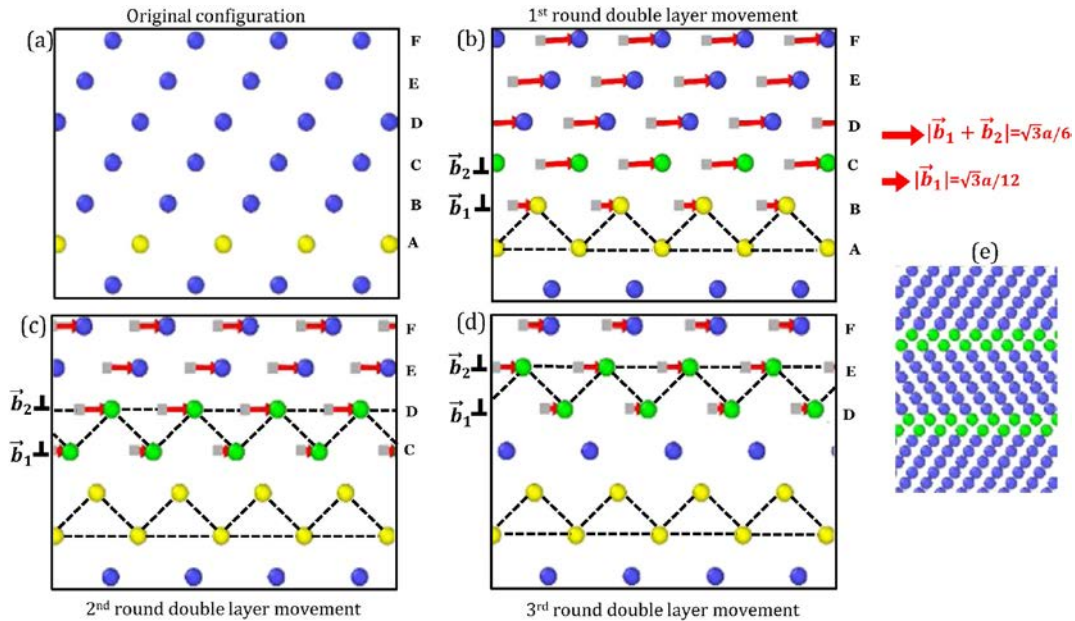
Fig. 2. Layer-by-layer movement of 1/12<111> dislocations ($\vec{b}_1$ and $\vec{b}_2$) on adjacent {112} planes. For each round of movement, the passage of a lower dislocation and an upper 1/12<111> dislocation is realized by displacing two blocks that differ in one layer of {112} atoms. From (a) to (d), the lower TB highlighted in yellow is fixed while the upper TB is subject to migrate. The isosceles triangular structure is delineated by dashed lines. Gray squares are used to represent atomic positions prior to the current round of displacement. Red arrows are displacement vectors for atom movement. Projection of a 7-layer twin is given in (e).

situated on adjacent {211} atomic layers. In the first step, the $\vec{b}_1$ dislocation glides and displaces the section BCDEF above it by $|\vec{b}_1|$ (Fig. 2b). This results into an isosceles triangular arrangement of atomic layers: each atom in Layer B is at a vertex position of an isosceles triangle, while atoms in Layer A become the triangle base side. In the second equivalent step, glide of $\vec{b}_2$ dislocation displaces the section labeled as CDEF by $|\vec{b}_2|$ to the right, with Layer B kept static. After this step, the section CDEF has displaced by $\frac{\sqrt{3}a}{6}$ in total and Layer B has displaced by $\frac{\sqrt{3}a}{12}$ (Fig. 2b). This twinning deformation continues when more 1/12<111> dislocations subsequently glide on upper atomic layers (Fig. 2c–d), causing continuous growth of a twin region that has the isosceles boundary (Fig. 2e). An animation detailing this process can be found in SM-III.

To understand which twinning behavior is activated more easily in a given BCC system, the generalized stacking fault energy (GSFE) curves for the two configurations were computed for the five BCC metals studied here. They are displayed in Fig. 3. In the case of Ta, Nb, and Fe, it was found that the stacking fault energy (γ^{sf}) needed to initiate the isosceles TB formation is smaller than that required for reflection TB formation, thus favoring an isosceles TB formation (Fig. 3a). For W, the reverse was determined to be true: the γ^{sf} value corresponding to isosceles structure formation is much larger than that for reflection TB (Fig. 3b). An interesting phenomenon was observed for Mo. For this case, even though γ^{sf} is lower for the initiation of an isosceles TB, its complete formation was determined to be energetically unfavorable. This is attributed to a large ($\gamma^{usf} - \gamma^{sf}$) value of 387 mJ/m^2 for the isosceles twin structure, where γ^{usf} is the unstable stacking fault energy, compared with 145 mJ/m^2 for the reflection twin structure (Fig. 3c). In order to confirm these trends, thermal stability of both isosceles and reflection TBs in the five metals was studied by isothermal relaxation, and it was found that an initial reflection TB will change to isosceles TB for Ta, Fe and Nb; while for Mo and W the opposite will occur (details in SM-V).

After the activation of twin structures, their stability is controlled by the stable twinning fault energy (γ^{stf}). The TB with a lower γ^{stf} is more likely to retain its configuration. The ratio of this parameter for the two competing mechanisms, $\gamma^{stf}_{iso}/\gamma^{stf}_{ref}$, suggests that isosceles TB is more stable in Ta, Nb, and Fe, while Mo and W would favor reflection TB (Table 1). Based on this analysis, the propensity for occurrence of isosceles TB was determined as Ta > Nb > Fe.

The above ranking was further verified by conducting a dislocation density analysis. The ratio of dislocation densities corresponding to the two TB structures, ρ_{iso}/ρ_{ref}, was traced for the TB migration process for the three NWs (Fig. 3d). The larger this ratio is for a specific BCC NW, the more 1/12<111> dislocations would exist during the NW deformation, implying a higher tendency for isosceles TB formation. From Fig. 3d, it is clear that Ta has the highest ρ_{iso}/ρ_{ref}, hence it would have the largest likelihood to realize isosceles TB. Nb comes in the second place in this regard, and Fe shows the lowest preference among the three NWs for isosceles TB formation. This result is in good agreement with the ranking deduced from the aforementioned GSFE analysis.

In summary, the present work reveals that twinning in BCC NWs can occur via forming the unconventional isosceles TB structure, which is attributed to the dissociation of initially nucleated 1/6<111> dislocation into two 1/12<111> partials and their subsequent glide on adjacent {211} planes. Competition between the two gliding mechanisms is analyzed by comparing GSFE curves associated with both isosceles and reflection TB structures. We conclude that Ta, Nb, and Fe NWs are more likely to have the double layer 1/12<111> dislocation glide as their dominant twinning mechanism; whereas W and Mo NWs are more likely to undergo twinning via 1/6<111> dislocation glide. Moreover, among the three BCC metals preferring isosceles TBs, this twinning mechanism could be ranked in decreasing order of probability of occurrence as: Ta > Nb > Fe, as is supported by a dislocation density analysis. The fundamental insight gained from this theoretical analysis provides better understanding of atomistic deformation mechanisms in BCC metals at the nanoscale, and would be valuable in realizing their latent strength in practical applications.
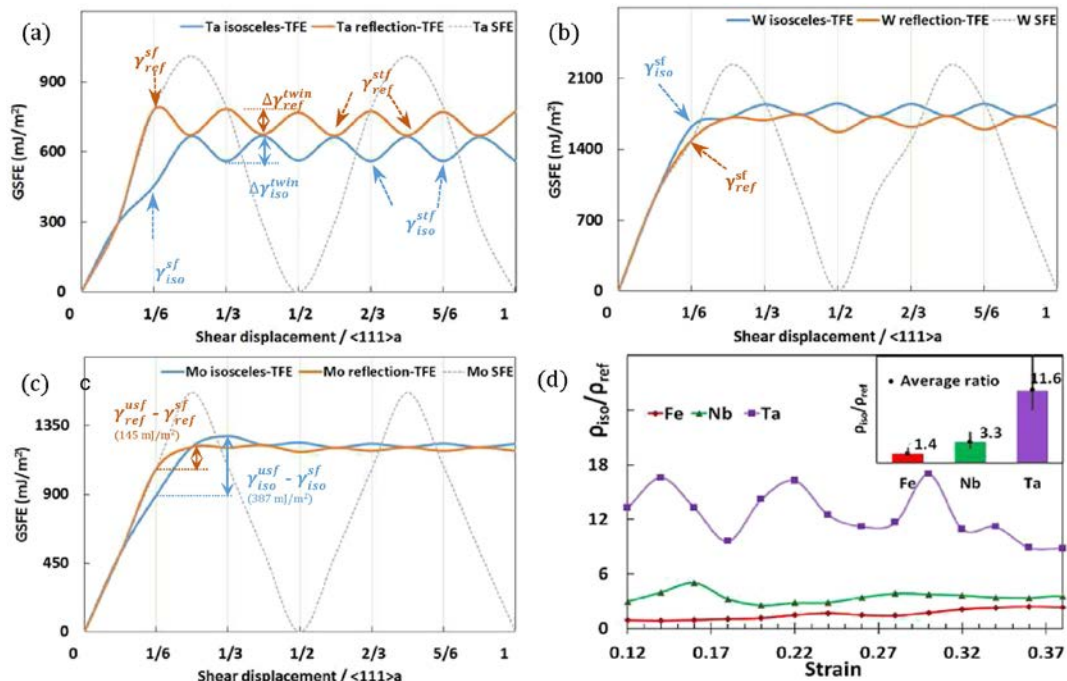
Acknowledgments

Fig. 3. GSFE curves for Ta, W, and Mo showing the competition of isosceles and reflection TB formation (a–c). (d) Density ratio ρ_{iso}/ρ_{ref} during TB migration process of Fe, Nb, and Ta NWs (T = 0.1 K, strain rate 10^7/s, <100>-oriented). Statistical range and arithmetic average of these ratios are embedded on top.

Table 1
Summary of energetics of TB migration via two competing twinning mechanisms in five BCC NWs, where γ_{TBM} denotes the energy barrier for TB migration, and γ^{stf} and γ^{utf} represent the stable and unstable twinning fault energies, respectively. The γ_{TBM} values match closely with the GSFE calculation performed in literature using DFT or MD.

	Ta		Nb		Fe		Mo		W	
	iso	refl	iso	refl	iso	refl	iso	refl	iso	refl
γ_{TBM} in mJ/m² (literature values)	102.7	103.3 (112 [12])	32	34.3 (47 [28])	35	37 (40 [28],32[12])	24	25.3 (34 [12],40 [29])	124.3	129.7 (130 [29])
$\gamma^{stf}_{iso}/\gamma^{stf}_{ref}$	**0.836**		**0.939**		**0.945**		**1.020**		**1.069**	
$\gamma^{utf}_{iso}/\gamma^{utf}_{ref}$	0.862		0.948		0.950		1.019		1.070	

Appendix A. Supplementary data

Supplementary data to this article can be found online at http://dx.doi.org/10.1016/j.scriptamat.2015.11.006.

References

[1] B. Wu, A. Heidelberg, J.J. Boland, Nat. Mater. 4 (2005) 525–529.
[2] M.D. Uchic, D.M. Dimiduk, J.N. Florando, W.D. Nix, Science 305 (2004) 986–989.
[3] G. Richter, K. Hillerich, D.S. Gianola, R. Mönig, O. Kraft, C.A. Volkert, Nano Lett. 9 (2009) 3048–3052.
[4] Y. Zhu, Q. Qin, F. Xu, F. Fan, Y. Ding, T. Zhang, B.J. Wiley, Z.L. Wang, Phys. Rev. B 85 (2012) 045443.
[5] C. Chisholm, H. Bei, M.B. Lowry, J. Oh, S.A. Syed Asif, O.L. Warren, Z.W. Shan, E.P. George, A.M. Minor, Acta Mater. 60 (2012) 2258–2264.
[6] H. Huang, H. Van Swygenhoven, MRS Bull. 34 (2009) 160–166.
[7] R. Maaß, S. Van Petegem, D. Ma, J. Zimmermann, D. Grolimund, F. Roters, H. Van Swygenhoven, D. Raabe, Acta Mater. 57 (2009) 5996–6005.
[8] J.R. Greer, J.T.M. De Hosson, Prog. Mater. Sci. 56 (2011) 654–724.
[9] T. Zhu, J. Li, Prog. Mater. Sci. 55 (2010) 710–757.
[10] J. Wang, Z. Zeng, C.R. Weinberger, Z. Zhang, T. Zhu, S.X. Mao, Nat. Mater. 14 (2015) 594–600.
[11] S. Li, X. Ding, J. Deng, T. Lookman, J. Li, X. Ren, J. Sun, A. Saxena, Phys. Rev. B 82 (2010) 205435.
[12] A. Cao, J. Appl. Phys. 108 (2010) (113531–113531–9).
[13] J. Zhu, D. Shi, J. Phys. Appl. Phys. 44 (2011) 055404.
[14] S. Li, X. Ding, J. Li, X. Ren, J. Sun, E. Ma, Nano Lett. 10 (2010) 1774–1779.
[15] V. Vítek, Scr. Metall. 4 (1970) 725–732.
[16] P.D. Bristowe, A.G. Crocker, M.J. Norgett, J. Phys. F: Met. Phys. 4 (1974) 1859.
[17] P.D. Bristowe, A.G. Crocker, Philos. Mag. 31 (1975) 503–517.
[18] L.M. Hsiung, D.H. Lassila, Scr. Mater. 39 (1998) 603–609.
[19] S. Nosé, J. Chem. Phys. 81 (1984) 511–519.
[20] G.J. Ackland, R. Thetford, Philos. Mag. A 56 (1987) 15–30.
[21] M.R. Fellinger, H. Park, J.W. Wilkins, Phys. Rev. B 81 (2010).
[22] M.I. Mendelev, S. Han, D.J. Srolovitz, G.J. Ackland, D.Y. Sun, M. Asta, Philos. Mag. 83 (2003) 3977–3994.
[23] R. Ravelo, T.C. Germann, O. Guerrero, Q. An, B.L. Holian, Phys. Rev. B 88 (2013).
[24] D.E. Smirnova, A.Y. Kuksin, S.V. Starikov, V.V. Stegailov, Z. Insepov, J. Rest, A.M. Yacout, Model. Simul. Mater. Sci. Eng. 21 (2013) 035011.
[25] D.H. Warner, W.A. Curtin, S. Qu, Nat. Mater. 6 (2007) 876–881.
[26] A. Stukowski, Model. Simul. Mater. Sci. Eng. 18 (2010) 015012.
[27] C.D. Hansen, C.R. Johnson (Eds.), The Visualization Handbook, Elsevier-Butterworth Heinemann, Amsterdam; Boston, 2005.
[28] A. Ojha, H. Sehitoglu, Philos. Mag. Lett. 94 (2014) 647–657.
[29] S. Ogata, J. Li, S. Yip, Phys. Rev. B 71 (2005) 224102.